The First JWST Spectrum of a GRB Afterglow: No Bright Supernova in Observations of the Brightest GRB of all Time, GRB 221009A

A. J. Levan[1,2] , G. P. Lamb[3] , B. Schneider[4] , J. Hjorth[5] , T. Zafar[6] , A. de Ugarte Postigo[7] , B. Sargent[8,9] ,
S. E. Mullally[8] , L. Izzo[5] , P. D'Avanzo[10] , E. Burns[11] , J. F. Agüí Fernández[12] , T. Barclay[13,14] , M. G. Bernardini[10] ,
K. Bhirombhakdi[8] , M. Bremer[15] , R. Brivio[10,16] , S. Campana[10] , A. A. Chrimes[1] , V. D'Elia[17,18] , M. Della Valle[19] ,
M. De Pasquale[20] , M. Ferro[10,16] , W. Fong[21] , A. S. Fruchter[8] , J. P. U. Fynbo[22,23] , N. Gaspari[1] , B. P. Gompertz[24] ,
D. H. Hartmann[25] , C. L. Hedges[13,14] , K. E. Heintz[22,23] , K. Hotokezaka[26] , P. Jakobsson[27] , D. A. Kann[28,44] ,
J. A. Kennea[29] , T. Laskar[1,30] , E. Le Floc'h[31] , D. B. Malesani[1,22,23] , A. Melandri[18] , B. D. Metzger[32,33] ,
S. R. Oates[24] , E. Pian[34] , S. Piranomonte[18] , G. Pugliese[35] , J. L. Racusin[36] , J. C. Rastinejad[21] , M. E. Ravasio[1,10] ,
A. Rossi[34] , A. Saccardi[37] , R. Salvaterra[38] , B. Sbarufatti[10] , R. L. C. Starling[39] , N. R. Tanvir[39] , C. C. Thöne[40] ,
A. J. van der Horst[41] , S. D. Vergani[37] , D. Watson[22,23] , K. Wiersema[42] , R. A. M. J. Wijers[35] , and Dong Xu[43]

[1] Department of Astrophysics/IMAPP, Radboud University, 6525 AJ Nijmegen, The Netherlands; a.levan@astro.ru.nl
[2] Department of Physics, University of Warwick, Coventry, CV4 7AL, UK
[3] Astrophysics Research Institute, Liverpool John Moores University, 146 Brownlow Hill, Liverpool L3 5RF, UK
[4] Kavli Institute for Astrophysics and Space Research, Massachusetts Institute of Technology, 77 Massachusetts Avenue, Cambridge, MA 02139, USA
[5] DARK, Niels Bohr Institute, University of Copenhagen, Jagtvej 128, DK-2200 Copenhagen, Denmark
[6] Australian Astronomical Optics, Macquarie University, 105 Delhi Road, North Ryde, NSW 2113, Australia
[7] Artemis, Université Côte d'Azur, Observatoire de la Côte d'Azur, CNRS, F-06304 Nice, France
[8] Space Telescope Science Institute, 3700 San Martin Drive, Baltimore, MD 21218, USA
[9] Center for Astrophysical Sciences, The William H. Miller III Department of Physics and Astronomy, Johns Hopkins University, Baltimore, Maryland 21218, USA
[10] INAF, Osservatorio Astronomico di Brera, via E. Bianchi 46, I-23807, Merate (LC), Italy
[11] Department of Physics and Astronomy, Louisiana State University, Baton Rouge, LA 70803 USA
[12] Instituto de Astrofísica de Andalucía—CSIC, Glorieta de la Astronomía s/n, E-18008 Granada, Spain
[13] NASA Goddard Space Flight Center, Greenbelt, MD 20771, USA
[14] University of Maryland, Baltimore County, Baltimore, MD 21250, USA
[15] Institut de Radioastronomie Millimétrique (IRAM), 300 Rue de la Piscine, F-38406 Saint Martin d'Hères, France
[16] Universitá degli Studi dell'Insubria, Dipartimento di Scienza e Alta Tecnologia, via Valleggio 11, I-22100 Como, Italy
[17] ASI, Italian Space Agency, Space Science Data Centre, Via del Politecnico snc, I-00133 Rome, Italy
[18] INAF, Osservatorio Astronomico di Roma, Via Frascati 33, I-00040 Monte Porzio Catone (RM), Italy
[19] Capodimonte Astronomical Observatory, INAF-Napoli, Salita Moiariello 16, I-80131 Napoli, Italy
[20] University of Messina, Mathematics, Informatics, Physics and Earth Science Department, Via F.D. D'Alcontres 31, Polo Papardo, I-98166, Messina, Italy
[21] Center for Interdisciplinary Exploration and Research in Astrophysics (CIERA) and Department of Physics and Astronomy, Northwestern University, Evanston, IL 60208, USA
[22] The Cosmic DAWN Center, Denmark
[23] Niels Bohr Institute, Copenhagen University, Jagtvej 155, DK-2200, Copenhagen N, Denmark
[24] School of Physics and Astronomy & Institute for Gravitational Wave Astronomy, University of Birmingham, Birmingham B15 2TT, UK
[25] Department of Physics and Astronomy, Clemson University, Clemson, SC 29634, USA
[26] Research Center for the Early Universe, Graduate School of Science, University of Tokyo, Bunkyo, Tokyo 113-0033, Japan
[27] Centre for Astrophysics and Cosmology, Science Institute, University of Iceland, Dunhagi 5, 107 Reykjavík, Iceland
[28] Hessian Research Cluster ELEMENTS, Giersch Science Center, Max-von-Laue-Straße 12, Goethe University Frankfurt, Campus Riedberg, D-60438 Frankfurt am Main, Germany
[29] Department of Astronomy and Astrophysics, Pennsylvania State University, 525 Davey Lab, University Park, PA 16802, USA
[30] Department of Physics & Astronomy, University of Utah, Salt Lake City, UT 84112, USA
[31] Université Paris-Saclay, Université Paris Cité, CEA, CNRS, AIM, F-91191, Gif-sur-Yvette, France
[32] Department of Physics and Columbia Astrophysics Laboratory, Columbia University, Pupin Hall, New York, NY 10027, USA
[33] Center for Computational Astrophysics, Flatiron Institute, 162 5th Avenue, New York, NY 10010, USA
[34] INAF, Osservatorio di Astrofisica e Scienza dello Spazio, via Piero Gobetti 93/3, I-40024, Bologna, Italy
[35] Astronomical Institute Anton Pannekoek, University of Amsterdam, 1090 GE Amsterdam, The Netherlands
[36] Astrophysics Science Division, NASA Goddard Space Flight Center, Greenbelt, MD 20771, USA
[37] GEPI, Observatoire de Paris, Université PSL, CNRS, 5 Place Jules Janssen, F-92190 Meudon, France
[38] INAF, Istituto di Astrofisica Spaziale e Fisica Cosmica, via Alfonso Corti 12, I-20133 Milano, Italy
[39] School of Physics and Astronomy, University of Leicester, University Road, Leicester, LE1 7RH, UK
[40] Astronomical Institute of the Czech Academy of Sciences, Fričova 298, 251 65 Ondřejov, Czech Republic
[41] Department of Physics, George Washington University, 725 21st Street NW, Washington, DC 20052, USA
[42] Physics Department, Lancaster University, Lancaster, LA1 4YB, UK
[43] Key Laboratory of Space Astronomy, National Astronomical Observatories, Chinese Academy of Sciences, Beijing, 100101, People's Republic of China

_____
[44] Deceased

Abstract

We present James Webb Space Telescope (JWST) and Hubble Space Telescope (HST) observations of the afterglow of GRB 221009A, the brightest gamma-ray burst (GRB) ever observed. This includes the first mid-IR spectra of any GRB, obtained with JWST/Near Infrared Spectrograph (0.6–5.5 micron) and Mid-Infrared Instrument (5–12 micron), 12 days after the burst. Assuming that the intrinsic spectral slope is a single power law, with $F_\nu \propto \nu^{-\beta}$, we obtain $\beta \approx 0.35$, modified by substantial dust extinction with $A_V = 4.9$. This suggests extinction above the notional Galactic value, possibly due to patchy extinction within the Milky Way or dust in the GRB host galaxy. It further implies that the X-ray and optical/IR regimes are not on the same segment of the synchrotron spectrum of the afterglow. If the cooling break lies between the X-ray and optical/IR, then the temporal decay rates would only match a post-jet-break model, with electron index $p < 2$, and with the jet expanding into a uniform ISM medium. The shape of the JWST spectrum is near-identical in the optical/near-IR to X-SHOOTER spectroscopy obtained at 0.5 days and to later time observations with HST. The lack of spectral evolution suggests that any accompanying supernova (SN) is either substantially fainter or bluer than SN 1998bw, the proto-type GRB-SN. Our HST observations also reveal a disk-like host galaxy, viewed close to edge-on, that further complicates the isolation of any SN component. The host galaxy appears rather typical among long-GRB hosts and suggests that the extreme properties of GRB 221009A are not directly tied to its galaxy-scale environment.

Unified Astronomy Thesaurus concepts: Gamma-ray bursts (629)

1. Introduction

Gamma-ray bursts (GRBs) are the instantaneously most luminous events known in the universe. They arise in at least two varieties, long and short (Kouveliotou et al. 1993), reflecting the typical durations of their prompt emission. The majority of long bursts are thought to arise from the collapse of very massive stars, an origin secured through observations of associated supernovae (SNe; Hjorth et al. 2003; Levan et al. 2016). Many of the short GRBs likely arise from the merger of compact objects, as evidenced by the presence of kilonova emission in their light curves (Berger et al. 2013; Tanvir et al. 2013; Gompertz et al. 2018; Lamb et al. 2019; Rastinejad et al. 2021), and most robustly by their association with a gravitational wave signal (Abbott et al. 2017). Although it should be noted that there is clearly a more significant overlap in the progenitors of long and short GRBs than previously realized, with SNe in some short GRBs (Ahumada et al. 2021; Rossi et al. 2022), and kilonovae in bursts with durations in excess of a minute (Mei et al. 2022; Rastinejad et al. 2022; Troja et al. 2022; Yang et al. 2022). GRBs have been used as probes of extreme physics, routes to understanding stellar evolution and as lighthouses to the distant universe.

The long-duration GRB 221009A is, by any measure, the brightest GRB to have been discovered in more than 50 yr of sky-monitoring and out of ∼10,000 GRBs. Rate estimates suggest bursts like it should occur only once every few centuries (Burns et al. 2023; Malesani et al. 2023; Williams et al. 2023). Furthermore, it is the first GRB to have emission detected at tens of teraelectronvolts (Dzhappuev et al. 2022; Huang et al. 2022), and its afterglow has been observed from the γ-ray to radio as part of intensive follow-up (e.g., Kann et al. 2023; Laskar et al. 2023; O'Connor et al. 2023; Williams et al. 2023). Critically, observations from the Very Large Telescope (VLT)/X-SHOOTER (de Ugarte Postigo et al. 2022b; Malesani et al. 2023), and subsequently the Gran Telescopio Canarias (GTC; Castro-Tirado et al. 2022) showed the redshift to be $z = 0.151$—a very local event by GRB standards.

Most bursts found at low redshifts have been low-energy events (e.g., Soderberg et al. 2006; Chapman et al. 2007), perhaps the result of a fundamentally different emission process (e.g., arising from shock breakout rather than directly from the relativistic jet itself; Campana et al. 2006; Waxman et al. 2007). Instead, the isotropic-equivalent energy release of GRB 221009A is $E_{\gamma,\mathrm{iso}} > 10^{54}$ erg, and comparable to the most energetic and distant GRBs seen at high redshift. Furthermore, the event's proximity is such that any associated SN, and its underlying host galaxy, are open to intensive study, offering the opportunity to test similarities between the substantially subluminous local GRB population and the much more luminous cosmological population. However, in the case of GRB 221009A, this is complicated by a location on the sky near the Galactic plane, where foreground extinction is both large ($A_V \sim 4.2$) and uncertain, where crowding complicates optical and IR observations. Even X-ray observations must contend with an additional contribution from the dust-scattered X-ray halo (Williams et al. 2023).

Despite these challenges, observations to date have yielded a rich data set across the electromagnetic spectrum (e.g., Fulton et al. 2023; Kann et al. 2023; Laskar et al. 2023; O'Connor et al. 2023; Shrestha et al. 2023; Williams et al. 2023). These data paint a complex picture of a burst with multiple components not readily subsumed within standard afterglow models. In addition, there are apparent detections of the associated SN 2022ixw (Fulton et al. 2023) and excess emission in the radio regime (Laskar et al. 2023).

Here we present a set of space-based, high spatial resolution observations of GRB 221009A obtained with the James Webb Space Telescope (JWST) and Hubble Space Telescope (HST). These minimize impacts from crowding, extend redward of the limit of ground-based observations, and provide the necessary spatial resolution to identify the host galaxy. Although they do not sample the temporal evolution of the event as well as the extensive observations from the ground, they are, in principle, substantially cleaner because of their high resolution and signal-to-noise ratio (S/N) and provide a well-sampled spectral energy distribution (SED). Therefore, we use them to probe the evolving SED of GRB 221009A, which is essential in understanding both the physics of the blast wave and the presence and properties of any associated SN.

2. Observations

Many space-based γ-ray observatories identified GRB 221009A. These included Fermi-GBM (Veres et al. 2022), Fermi-LAT (Bissaldi et al. 2022), AGILE/MCAL (Ursi et al.
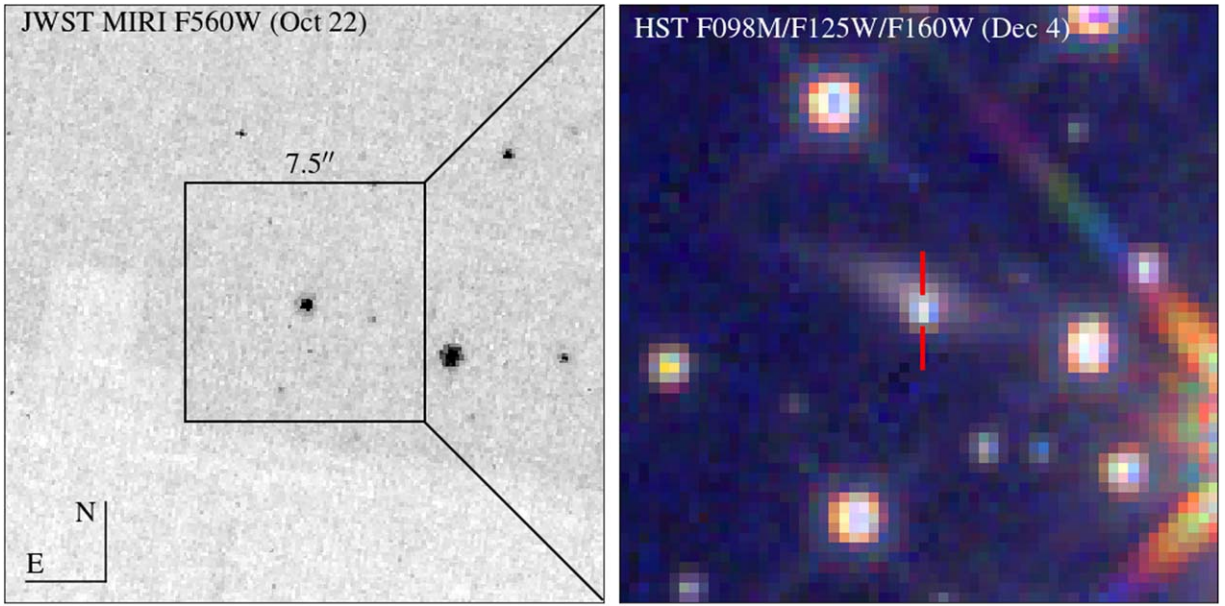
Figure 1. The field of GRB 221009A as imaged for target acquisition for the JWST spectroscopy on October 21 (left), and later time observations with HST in the F098M/F125W and F160W filters (right). Only a short sequence was obtained for JWST, while the HST observations are substantially deeper. These observations clearly show the host galaxy of GRB 221009A extending to the NE and SW of the afterglow position.

2022), AGILE/GRID (Piano et al. 2022), INTEGRAL (Gotz et al. 2022), Konus-Wind (Frederiks et al. 2022) Insight-HMXT (Tan et al. 2022), STPSat-6/SIRI-2 (Mitchell et al. 2022), SATech-01/GECAM-C HEBS (Liu et al. 2022), SRG/ART-XC (Lapshov et al. 2022), Solar Orbiter/STIX (Xiao et al. 2022), and GRBalpha (Ripa et al. 2022). The initial brightness seen by the Neil Gehrels Swift Observatory (Swift) was sufficiently extreme (and also considering its on-sky location in the plane of the Milky Way) that it was proposed to be a new Galactic transient rather than a GRB, despite the fact that Swift triggered on the afterglow emission (Dichiara et al. 2022)

Following the identification of the source as a GRB (Kennea et al. 2022), ground-based observations rapidly secured a redshift measurement of $z = 0.151$ (de Ugarte Postigo et al. 2022b; Malesani et al. 2023). X-ray and optical observations continued until the source entered Sun-block and found a typical GRB afterglow decay. The optical data also showed evidence for emission from an accompanying SN (Fulton et al. 2023), although, as we will discuss in Section 3.3.1, isolation of such an SN component is challenging.

2.1. James Webb Space Telescope

On 2022 October 22, we obtained observations of the afterglow of GRB 221009A with JWST (program GO 2782, PI Levan). A single, uninterrupted set of observations were obtained with the Near Infrared Spectrograph (NIRSPEC; Jakobsen et al. 2022) and Mid-Infrared Instrument (MIRI; Rieke et al. 2015). NIRSPEC observations began at 17:13 UT and MIRI at 18:12, corresponding to times since burst of 13.16 and 13.20 days, respectively. An image of the field at the time is shown in Figure 1, and the resulting spectra are shown in Figure 2.

For NIRSPEC, we utilized the prism, spanning a spectral range from 0.5–5.5 μm at a low (and variable) spectral resolution. The MIRI observations were undertaken in low-resolution mode and span the 5–12 μm range. For both

NIRSPEC and MIRI observations, we reprocessed the data with the most up-to-date calibrations from 2022 December and obtained 1D extractions. Comparing these products with those obtained from the archive processing shows good agreement; however, our re-reduction of the NIRSPEC data is ~10% brighter beyond 5 μm than the archival data. This reprocessing provides more consistent spectral fits between MIRI and NIRSPEC (see below), although it also introduces a small disjoint at the overlap region (see Figure 2).

In addition to spectroscopy, a short (11 s) acquisition image was also obtained in F560W with MIRI, as shown in Figure 1. This provides a photometric measurement at this epoch of F560W(AB) = 17.9 ± 0.1. For NIRSPEC data, we used near-simultaneous observations taken with the 3.6 m Italian Telescopio Nazionale Galileo (TNG) to check the calibration in the J, H, and K bands. The match appears excellent, so we adopt the flux calibration direct from the pipeline without additional scaling.

2.2. Supporting Observations

In order to build a simultaneous SED at the time of the JWST observations, we utilize the Swift-XRT data, as well as obtain observations at the 10.4 m GTC in the optical, the 3.6 m Italian TNG in near-infrared (NIR), and the Northern Extended Millimetre Array (NOEMA) in the millimeter regime.

The GRB was observed with the OSIRIS instrument on the GTC 1 day after the JWST observation, 14.31 days after the burst (program GTCMULTIPLE2M-22B, PI Kann). The observations consisted of both imaging in g, r, i, and z and spectroscopy. We perform a small correction in the photometry by using the observed temporal decay slope measured from the light curve to derive the photometry at the time of the JWST spectra. The OSIRIS spectroscopy consisted of 4×1200 s exposures with the R1000B grism, which covers the spectral range between 3700 and 7800 Å at a resolving power of $R \approx 600$.
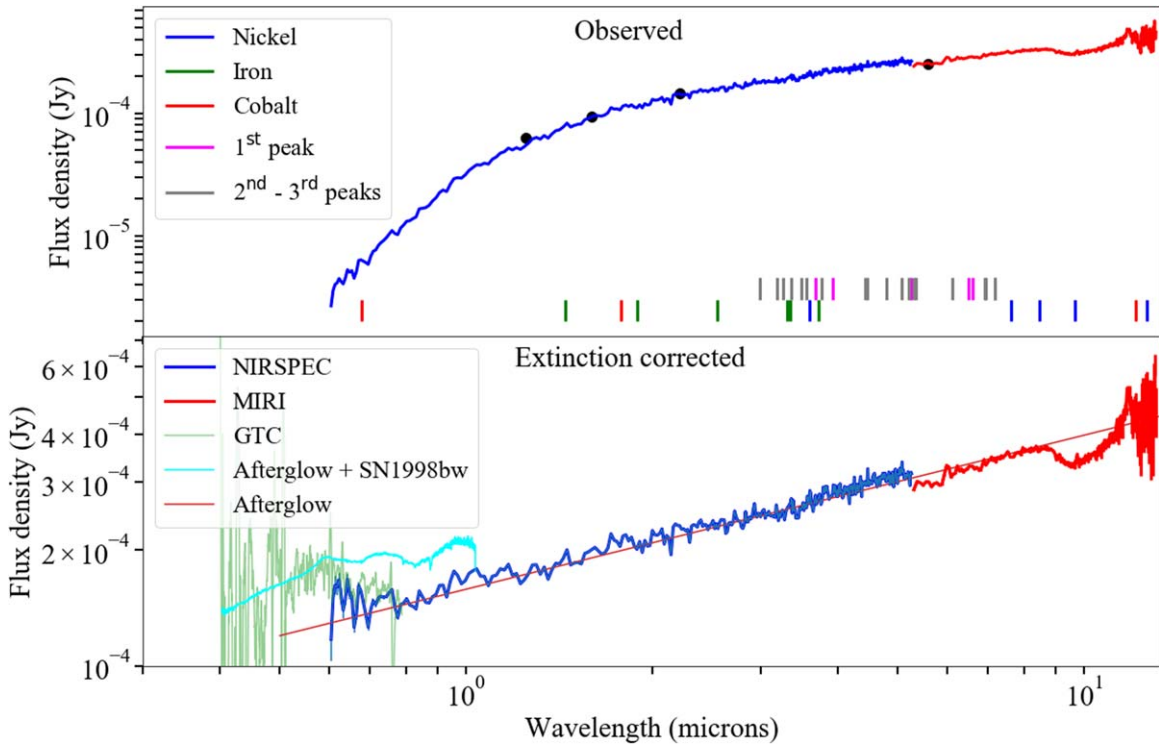
Figure 2. The JWST NIRSPEC+MIRI spectrum of GRB 221009A as observed at 12 days post-burst. The upper panel shows the observed spectrum (with the black points showing near-simultaneous photometry), while the lower panel is corrected for a foreground extinction of $A_V = 4.9$. While this has little impact on the mid-IR, the correction factors for the optical are a factor of ~100. The spectrum appears largely featureless, although some possible absorption features are seen. At this epoch, there are no individual emission features. For comparison, expected lines from iron group elements and possible $r-$ process contributions are marked (Hotokezaka et al. 2022). For comparison, we also plot the best-fit absorbed power-law model and how SN 1998bw at 12 days would appear in addition to that model (the SN should contribute minimally at >5 μm, such that this additive approach is reasonable). The spectrum does not require the presence of any additional component. However, the bluest regions (which are also those most impacted by the extinction correction) do show an upturn, which is apparently also present in GTC observations. This upturn could be indicative of some SN contribution in the blue.

NIR observations of GRB 221009A were carried out with the TNG telescope using the NICS instrument in imaging mode. Here we use observations carried out on October 22, approximately 13.3 days after the burst, and nearly simultaneous with the JWST observation. The image reduction was carried out using the JITTER task of the ESO-ECLIPSE package.[45] Astrometry was performed using the Two Micron All Sky Survey (2MASS)[46] catalog. Aperture and point-spread function (PSF)-matched photometry were performed using the DAOPHOT package (Stetson 1987). To minimize any systematic effect, we performed differential photometry with respect to a selection of local isolated and nonsaturated reference stars from the 2MASS and the UKIDSS[47] surveys. The resulting magnitudes in the AB-system are $J = 19.41 \pm 0.06$, $H = 18.97 \pm 0.06$, and $K = 18.49 \pm 0.08$ at 13.25 days post-burst.

A set of millimeter data taken with NOEMA between 78 and 150 GHz (program S22BF, PI de Ugarte Postigo) were interpolated to the epoch of the JWST observation. The observations were performed in the medium-extended C configuration. The data reduction and analysis was done with CLIC and MAPPING from the GILDAS software package, flux calibration was relative to the reference sources MWC349 and LKHA101. The fluxes were determined with UV point-source fits for a consistent error propagation. A full analysis of the NOEMA data set will be published in a forthcoming paper.

In addition to data taken nearly simultaneously with JWST, we also utilized the observations with VLT/X-SHOOTER obtained at 0.5 days post-burst (Malesani et al. 2023), since these provide an ideal comparison epoch where the source should be dominated by purely afterglow emission (i.e., the epoch is so early and the afterglow so bright that there should be no SN emission). The data reduction is described in detail in Malesani et al. (2023).

2.3. Hubble Space Telescope

We obtained three epochs of imaging with the HST on 2022 November 8, 2022 November 19, and 2022 December 4 (Program 17264, PI: Levan), corresponding to $\sim$30, 41, and 56 days post-burst. At the first epoch, observations were obtained in F625W, F775W, F098M, F125W, and F160W. A guide star failure in the IR observations during the second epoch meant that observations were only obtained in the optical. At the final observations on December 4, we obtained F625W, F098M, F125W, and F160W. The data were aligned and reduced via astrodrizzle, while the native pixel scale was retained due to the relative paucity of dithers in most cases (0″04 pix^{-1} for WFC3/UVIS images and 0″13 pix^{-1} for WFC3/IR images).

The images clearly show the afterglow in all bands superimposed on an underlying host galaxy. This host galaxy contributes modestly at the time of the first epoch but more than 50% of the light in 1″ apertures at later times. Ultimately, the optimal way to remove the host contribution would be via the direct subtraction of late-time images. However, given the
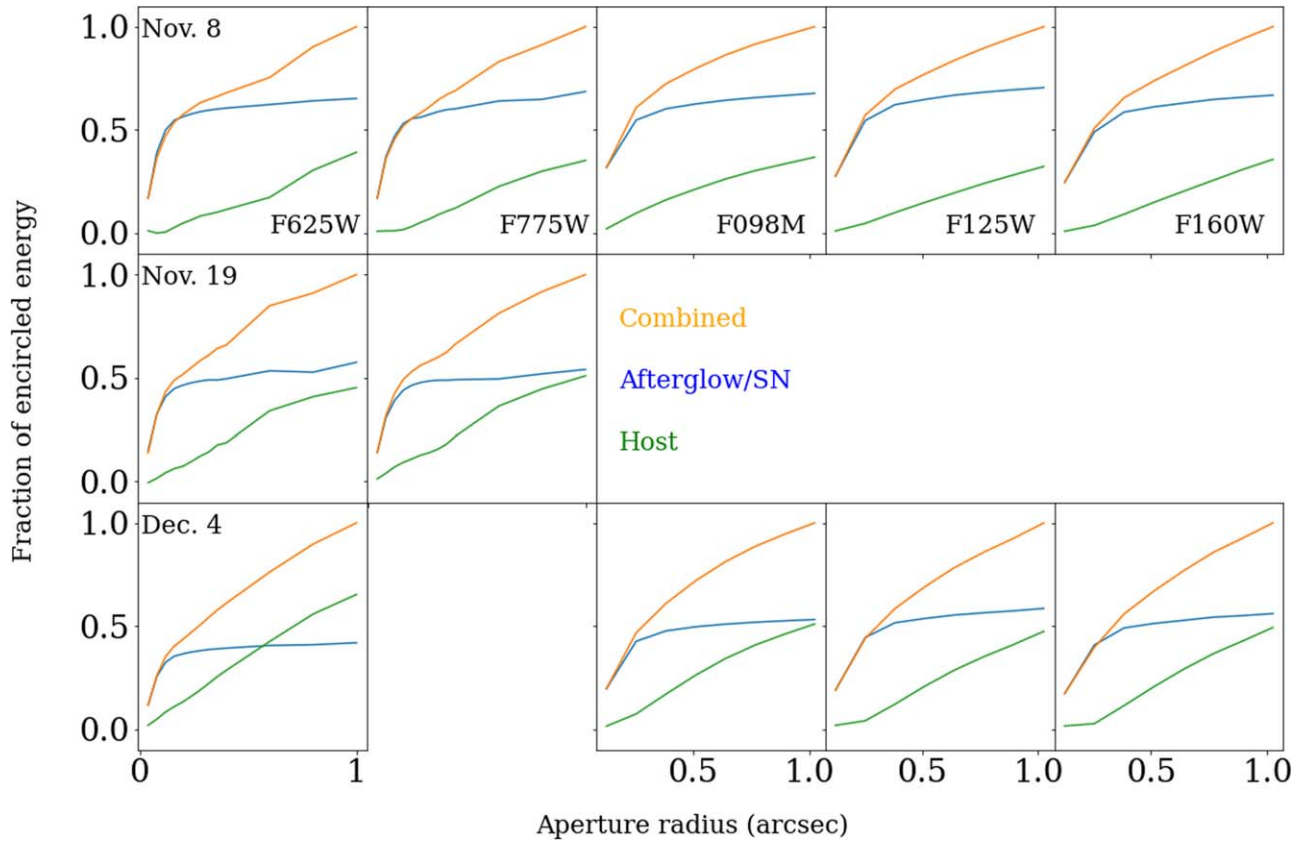

Figure 3. Radial profiles of the afterglow and host of GRB 221009A and their decomposition. The orange line shows the observed radial profile. The blue line is a stellar source from the field, scaled to the central regions such that the residual in the central $\sim 0\rlap{.}{''}1$ is comparable to the flux value in a region of the host at a similar offset to the GRB. The green line shows the residual following the subtraction of that point source, and represents the host galaxy light. The panels are normalized to the total enclosed counts within a $1''$ aperture around the afterglow position.

brightness of GRB 221009A, the afterglow contribution may remain detectable to HST for several years. We, therefore, report photometry via three different approaches.

First, we measure the curve of growth around the afterglow location, compared to that of an isolated star within the image (see Figure 3). We then scale the PSF and subtract it. In undertaking this subtraction, we consider the case where all of the light at the afterglow position is provided by the afterglow (i.e., we subtract to zero) and where there is an underlying contribution from the host galaxy. We estimate this contribution by measuring the flux in a small aperture at a location on the host that is a comparable distance from the center as the afterglow. We assign this value as our best estimate of the actual afterglow flux and set the error as the difference between this and zero (when applied symmetrically, this allows for either no underlying host contribution or a relatively bright underlying star-forming region). We believe this provides a conservative error estimate for the actual afterglow/SN brightness at any given epoch and note that this error is substantially larger than the photon counting/background errors introduced via the photometry (which are typically <1%).

Second, we also report measurements made in a larger ($1''$) aperture. This is the largest aperture that can be used without introducing significant additional light from other sources in the crowded field of view. These magnitudes are comparable to those measured from the ground and may be helpful for ground-based comparisons.

Finally, the unambiguous detection of the host galaxy in the F098M, F125W, and F160W filters at the last HST epoch (Figure 1) provides a different approach to decomposing the emission through modeling the light profile of the host. To model the system, we use a parametric method based on GALFIT (Peng et al. 2010) to simultaneously fit a Sérsic function for the host and a PSF component for the afterglow (see Schneider et al. 2022, for more details on the method). In addition, we also exploit the available multiwavelength images of the host to perform a multiband fit and derive a more robust wavelength-dependent model. This model is derived using GALFITM (Häußler et al. 2013; Vika et al. 2013), an extended multiband version of GALFIT where each component parameter is replaced by a polynomial function of wavelength. GALFITM is expected to provide a more consistent and homogeneous model of the object over wavelength and improve the information extracted from lower-S/N bands.

First, we ran GALFITM to simultaneously model the infrared filters (F098M, F125W, and F160W) of the final observation epoch (December 4). For the Sérsic function parameters, we consider a common position (x_c, y_c), axis ratio (b/a), and position angle (PA) for the three filters and let them vary as a constant offset from the input value. The half-light radius (also known as the effective radius and denoted as R_e) and Sérsic index (n) are defined as a linear function of the wavelength, while the magnitude is defined as a completely free parameter. Similarly, we use a PSF model with a free magnitude and a constant position as a function of the wavelength for the afterglow. Relaxing these assumptions does not strongly affect
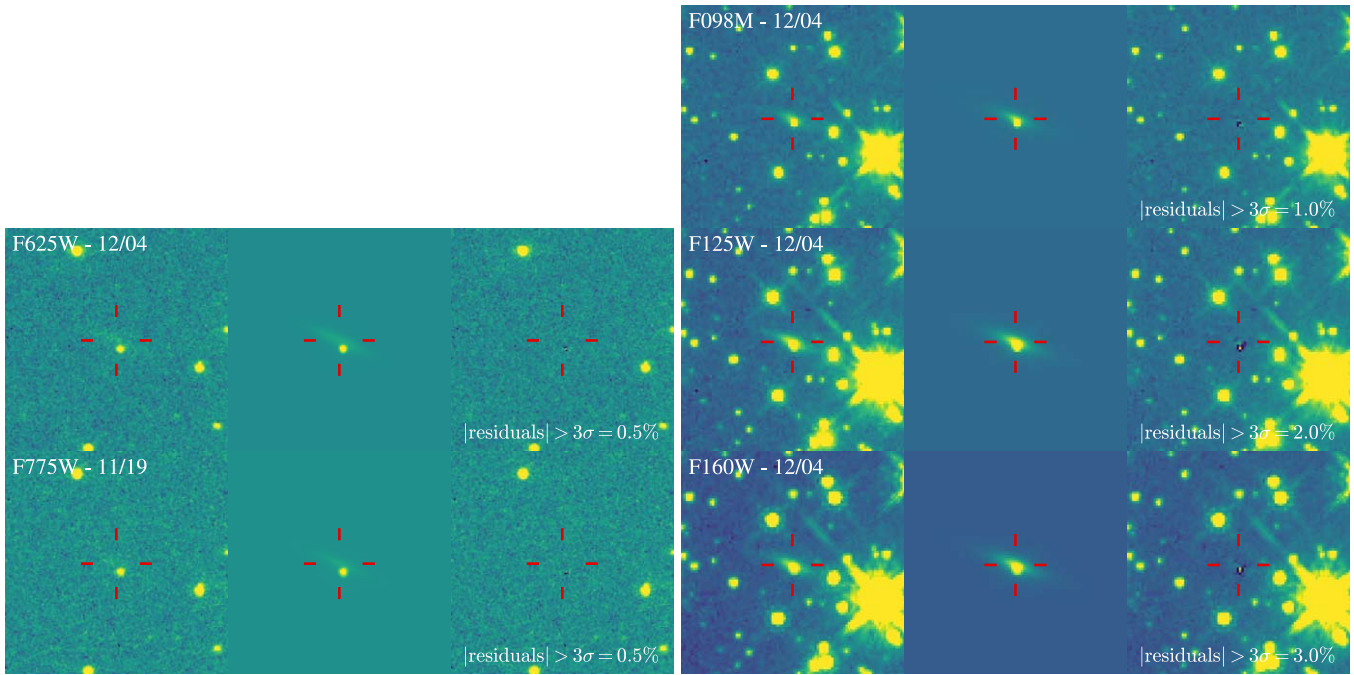
Figure 4. The five HST data sets used to decompose the host and afterglow light. Each panel row corresponds to a different filter with HST images of the GRB 221009A field on the left, the best-fit GALFITM models in the middle, and the residual maps on the right. Panels are centered on best-fit host positions and oriented with north pointing up and east pointing to the left. A common color scale is considered for a given row. The UVIS (left part) and IR (right part) filters correspond to a square region of $6''$ and $12''$, respectively. The fraction of pixels with a residual larger than 3σ within a constant $1''$ aperture radius is shown in the lower part of the residual map.

our estimates, especially for the magnitudes, R_e, and Sérsic index.

We adopted a similar approach to fit the HST/UVIS filters simultaneously. However, only F625W observations were secured during the last HST observations. We instead consider the November 19 observation for the F775W filter. Given that only the afterglow magnitude is expected to vary significantly between the two epochs, the observational delay on the host galaxy model should be limited. It is worth noting that the exposure time of F625W is about five times longer than F775W exposure and thus provides a deeper and higher-S/N image to drive and model the host through GALFITM. As a sanity check, we also run GALFIT on each filter individually. We find consistent host models with those of GALFITM, except for F775W, which converges to a different solution. This is likely due to the higher Galactic extinction that affects the host emission at this wavelength. The best-fit models and residual maps determined by GALFITM for the five HST filters are shown in Figure 4. A visual inspection of the residual maps confirms that we successfully reduced the majority of the initial flux of the system. More quantitatively, we consider a constant $1''$ radius aperture at the host position to measure the fraction of pixels above 3σ before and after the subtraction. We find that this fraction is reduced by more than 90% for all bands. We also note the presence of a marginal over-subtracted signal for the IR filters at the afterglow position. This might be caused by the central core of the PSF model used for the fit or by the presence of a compact and unresolved active star-forming region at the burst location, frequently observed for long-GRB host galaxies (e.g., Fruchter et al. 2006; Lyman et al. 2017).

Once the best-fit model of the host galaxy was determined, we used it as a constant input for all HST images. We thus run

GALFIT with a constant[48] Sérsic model for the host plus a free PSF model for the burst. The afterglow magnitudes derived from this approach are reported in Table 2, and we believe these to be the most robust estimates of the afterglow magnitudes at these epochs. The structural parameters of the host are further discussed in Section 4.

3. Spectral Shape and Evolution

3.1. Optical to Mid-IR Spectral Shape

We first consider the spectral shape observed in the NIRSPEC and MIRI data. The calibration appears robust, with the NIRSPEC observations matching ground-based JHK observations. The normalization of the MIRI data is consistent with the F560W acquisition image.

The spectrum is highly absorbed due to a significant Galactic foreground. This manifests as a strong suppression of the optical flux, while silicate features are also visible in the MIRI band at 8–10 μm. The strength of these silicate features likely varies on different lines of sight, and straightforward extinction laws do not remove it. Therefore, the region of the spectrum between $\sim$3 and 8 μm is likely to be least affected by Galactic extinction and can provide an estimate of the spectral slope. Indeed, this appears to be blue with $\beta \sim 0.4$ (defined as a power law with $F_\nu \propto \nu^{-\beta}$). This is much bluer than the X-ray spectral slope $\beta = 0.91 \pm 0.09$ at approximately the same time (Williams et al. 2023). This would be consistent with the presence of the cooling break between the two bands, although the very blue spectral slope is not naturally expected.

---

[48] More precisely, we let the host component vary within the uncertainties of the best-fit model.
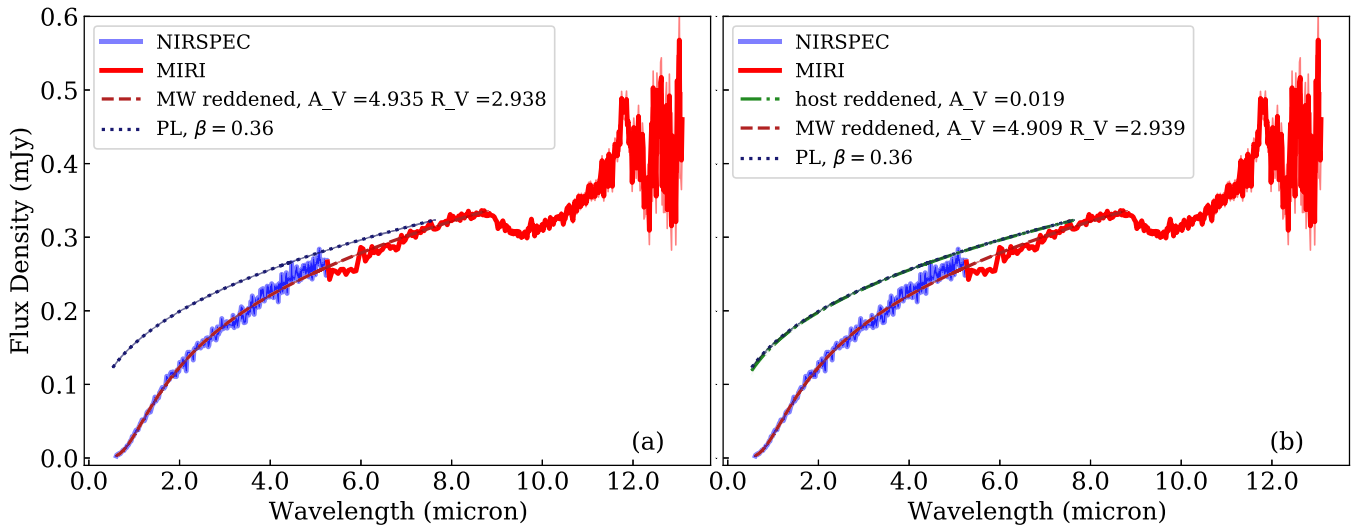
Figure 5. Fits found via MCMC for the two models: (a) a power law plus Milky Way extinction; and (b) a power law plus host galaxy and Milky Way extinction.

We perform a joint fit to the NIRSPEC and MIRI observations to better quantify the spectrum. We perform fits for two models: (a) a power law plus Milky Way (MW) extinction; and (b) a power law plus host galaxy and MW extinction. We set priors on the model parameters of $0.0 \leqslant \beta \leqslant 1.0$ for the power-law spectral index. We allow for a wide range of extinction within the MW $(0.0 \leqslant A_{V,\mathrm{MW}} \leqslant 10.0)$ and allow the fit to identify the best value given the condition $A_V \geqslant R_V E(B-V)$. We take the $A_V/E(B-V) = 2.742$ from Table 6 in Schlafly & Finkbeiner (2011), and using an initial $A_V = 4.17$, we find $E(B-V) = 1.52$. This value is used to set the maximum possible R_V for a given A_V such that $0.0 < R_V \leqslant A_V/E(B-V)$. In case (b), the prior on the host extinction is drawn from an exponential distribution, $P(A_{V,\mathrm{host}}) \propto \exp[-A_{V,\mathrm{host}}/0.3]$ (e.g., Holwerda et al. 2015), with a fixed $R_V = 2.93$, and the MW extinction is the same as that in case (a).

For both the Milky Way and the host galaxy, we use a Fitzpatrick (1999) extinction curve at $z = 0.0$ and $z = 0.151$, respectively. The models are fitted to the observed spectrum at wavelengths < 8.8 μm, to avoid any bias in the fits due to a more complex extinction feature at longer wavelengths. Figure 5, plotted against the joint data, shows our resultant spectral fits. Both models give a good approximation to the observed spectral shape, and the total extinction is consistent between them. The posterior distribution for model (b) shows a tight correlation between the Milky Way and host extinction, indicative of a degeneracy between these parameters. The extinction parameter and spectral index values from the Markov Chain Monte Carlo (MCMC) are shown in Table 1.

We note that the NIRSPEC and MIRI spectra have a statistically significant but modest difference in the preferred power-law index. By fitting a broken power-law model to the joint spectrum for NIRSPEC and MIRI, at < 8.8 μm, we find a best-fit model, using a reasonably sharp transition in a smoothly broken power law. The break is found at $\lambda \sim 4.46$ μm, and with a power-law index below the break, i.e., at shorter wavelengths, of $\beta = 0.40$, and above the break, longer, of $\beta = 0.32$. The sharpness of this break, its near coincidence with the point where the two spectra join, and the short wavelength range for the fit, especially with the MIRI data, suggest this difference, although statistically significant, is

Table 1
MCMC Posterior Parameter Values for Models (a), and (b), Fit to the JWST/ NIRSPEC and MIRI Spectrum at ~ 13 days

Model	β_1	R_V	$A_{V,\mathrm{MW}}$	$A_{V,\mathrm{host}}$
(a)	$0.362^{+0.001}_{-0.001}$	$2.938^{+0.008}_{-0.008}$	$4.935^{+0.006}_{-0.006}$	$\cdots$
(b)	$0.362^{+0.001}_{-0.001}$	$2.939^{+0.008}_{-0.008}$	$4.909^{+0.019}_{-0.040}$	$0.019^{+0.030}_{-0.014}$

Note. Columns are: the source power-law spectral index, β, the Milky Way extinction, $A_{V,\mathrm{MW}}$, and the host galaxy extinction, $A_{V,\mathrm{host}}$.

unlikely to be related to a physical change in the source spectrum. We, therefore, use the single power-law results.

We also fit identical models to the X-SHOOTER spectrum obtained at ~ 0.5 day post-burst and presented in Malesani et al. (2023). This spectrum is dominated entirely by the afterglow (no contribution from either an SN or host galaxy). It yields $\beta = 0.207$, $A_V = 4.903$, and $R_V = 3.225$, broadly comparable to the extinction values obtained from the JWST observations, although with a notably bluer spectral slope. However, we also note that, observationally, the spectra appear extremely similar (see Figure 6), and the differing values may reflect the lack of redder coverage for the X-SHOOTER observations.

By introducing a blackbody component with a limited temperature range and a broad luminosity distribution, i.e., consistent with the expectation from an SN, we can find a limit on the potential SN contribution to this spectrum. The fits return a strong correlation between maximum luminosity and the blackbody temperature, where higher temperatures allow for a higher maximum luminosity with the minimum luminosity defined by the prior. The fits that have an SN-like blackbody temperature, $T_{\mathrm{eff}} \gtrsim 5000$ K, return luminosities around $< 10^{42}$ erg s^{-1} (approximately 10%–20% of SN 1998bw at the same epoch; Nakamura et al. 2001). We note that the presence of a component with luminosity similar to SN 1998bw should result in a significant enhancement in the optical regime (see Figure 2). Therefore, the best model to describe the JWST spectrum of GRB 221009A has no measurable contribution from a thermal, SN-like component. However, we cannot rule out the possibility of a very blue SN, to which our observations have minimal sensitivity.
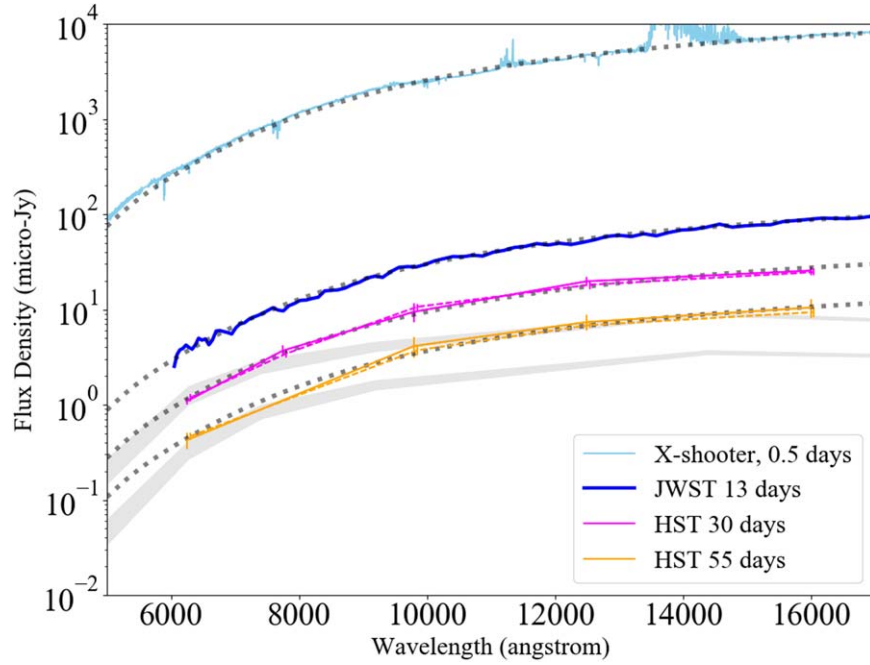
Figure 6. The evolution of the SED of the GRB 221009A afterglow from 0.5–55 days. The figure shows a 0.5 day X-SHOOTER spectrum, the 12 day JWST spectrum, and HST observations at 30 and 55 days. The solid and dashed lines refer to the decomposition of GALFIT estimates of the point-source magnitude and have been slightly offset in wavelength for clarity. The dashed line shows our best-fit absorbed power-law model (for a single Galactic extinction fit to our JWST spectrum). As can be seen, there is no evidence for spectral evolution between 0.5 and 12 days, indicating no significant SN contribution at this time. At later times, the uncertainty in the underlying host galaxy light dominates the HST observations and precludes drawing firm conclusions. However, it also does not support the presence of a bright SN component. The shaded gray areas show the SED of SN 1998bw at comparable epochs, representing a range of possible extinction from $A_V = 4.2$–4.9 mag. The dotted lines show the shape of the afterglow as determined from our JWST observations, but scaled to the other epochs. They demonstrate the possible changes in spectral shape from 0.5–55 days.

Table 2
HST Observations of GRB 221009A

Date	MJD	Δt (d)	Band	Exp.(s)	Point Source	$1''$ Aperture	GALFIT
2022-11-08:06:32:47	59891.27277367	29.72	F625W	960	23.81 ± 0.08	23.13 ± 0.07	23.72 ± 0.09
2022-11-08:06:41:33	59891.27886145	29.73	F775W	750	22.48 ± 0.13	21.97 ± 0.05	22.56 ± 0.09
2022-11-08:08:08:26	59891.33919124	29.79	F125W	798	20.66 ± 0.11	20.26 ± 0.02	20.75 ± 0.11
2022-11-08:08:15:37	59891.34417976	29.79	F098M	898	21.46 ± 0.22	20.91 ± 0.02	21.33 ± 0.07
2022-11-08:08:23:41	59891.34978161	29.80	F160W	798	20.38 ± 0.10	19.87 ± 0.01	20.42 ± 0.08
2022-11-19:04:58:39	59902.18082923	40.63	F625W	960	24.14 ± 0.11	23.44 ± 0.07	24.20 ± 0.16
2022-11-19:05:06:15	59902.18691700	40.63	F775W	750	23.15 ± 0.23	22.32 ± 0.12	23.04 ± 0.16
2022-12-04:02:02:24	59917.05554104	55.50	F625W	3776	24.83 ± 0.20	23.75 ± 0.10	24.73 ± 0.08
2022-12-04:22:03:49	59917.84907676	56.30	F125W	698	21.73 ± 0.25	20.91 ± 0.02	21.81 ± 0.06
2022-12-04:22:11:50	59917.85348639	56.30	F098M	898	22.36 ± 0.19	21.53 ± 0.04	22.47 ± 0.12
2022-12-04:22:18:14	59917.85908824	56.31	F160W	698	21.35 ± 0.23	20.49 ± 0.02	21.47 ± 0.08

Note. Photometry of the counterpart of GRB 221009A as observed with HST. The different magnitude columns are for the afterglow magnitude as derived via decomposition of a point and extended source, those measured in a large aperture, and the point-source magnitudes from GALFIT.

3.2. A Simultaneous Multiwavelength SED

In addition to our JWST observations, we also build a near-simultaneous broader band SED using X-ray data from the Swift-XRT (see also Williams et al. 2023), our GTC spectroscopy and NOEMA millimeter data. Extrapolating the X-ray flux and spectral slope confirms that a break is required between the X-ray and optical/IR regime. The difference in the measured spectral slopes is $\Delta\beta \sim 0.5$, consistent with interpreting this break as the cooling break. This model is shown in Figure 7.

The millimeter photometric points appear broadly consistent with the extrapolation of the $\beta = 0.35$ slope to this regime.

However, a single component from the optical to millimeter is disfavored due to the different temporal behavior of these regimes (see Laskar et al. 2023).

3.3. Line Features

In addition to mapping the overall afterglow, we may also expect to observe broad spectral features in these observations related to either the expected underlying SN emission or the presence of r-band nucleosynthesis, which is suggested to occur in the accretion disks formed during long GRBs (Siegel et al. 2019; Barnes & Metzger 2022). In Figure 2, we plotted the JWST spectrum and marked the locations of prominent iron
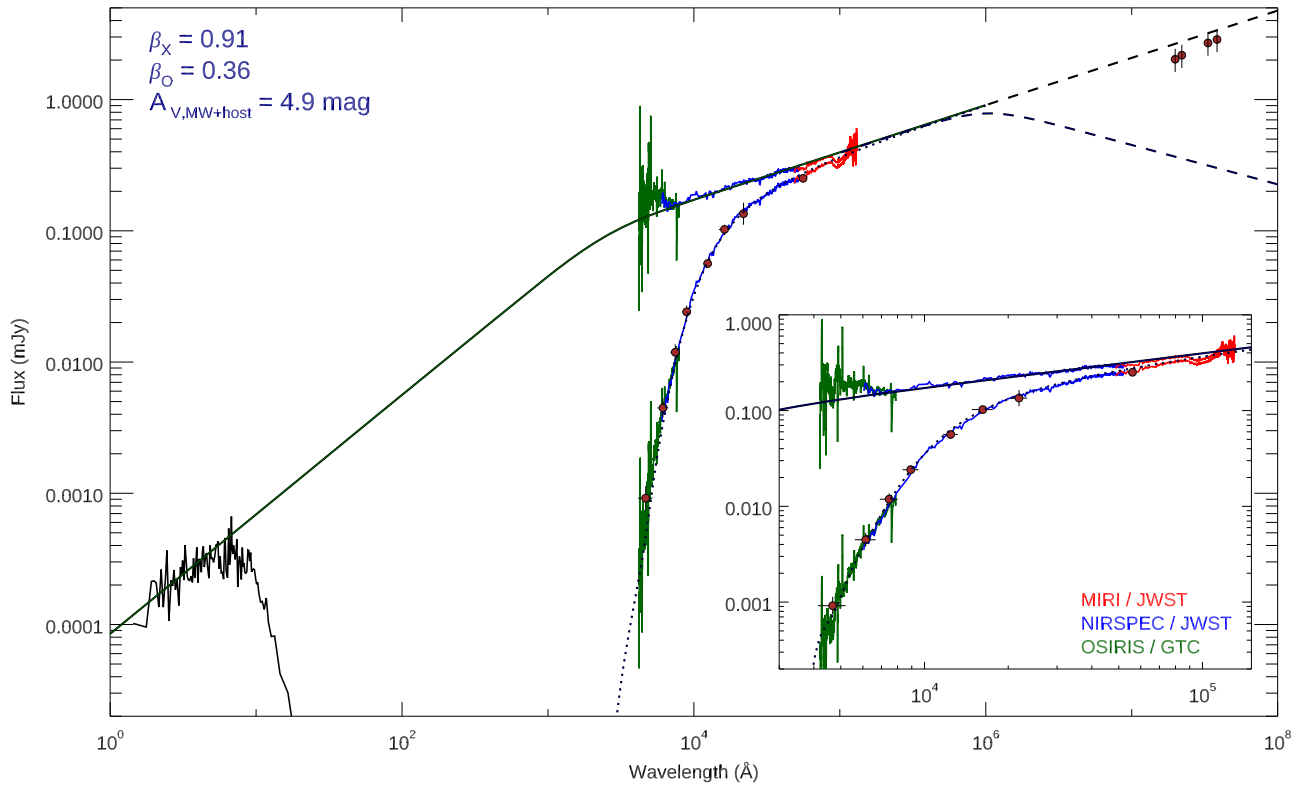
Figure 7. The X-ray (Swift-XRT to radio; NOEMA) SED of GRB 221009A at the time of the JWST observations. Solid lines show the underlying model, while the dotted lines are the observed points, with a strong deviation due to the heavy foreground extinction. Redward of the JWST observations, we show two possible models: one in which the peak frequency lies just beyond the JWST band (e.g., Laskar et al. 2023), and one that extends the JWST spectral slope out toward the radio regime. Interestingly, the continuation of the JWST spectrum is close to the millimeter points, as expected from our favored afterglow scenario (see Section 5.1).

group lines seen in SNe, in addition to suggested *r*-process lines from Hotokezaka et al. (2022). There are no apparent lines visible in the spectrum. This can be understood as a consequence of the early time of the observations. First, at this epoch, the SN (if present) is likely not optically thin, and heavier element lines (e.g., in particular, those from the *r*-process) may only be visible in the case of substantial mixing. Second, most (if not all) of the light observed via JWST is from the afterglow, not the SN component.

We note the presence of an apparent feature at ~ 11.8 μm in the MIRI band. This would be consistent with a blueshifted [Co II] line—a line that was strikingly the strongest observed feature in the mid-IR spectrum of SN 1987A (Aitken 1988). However, an inspection of the 2D MIRI images, before spectral extraction, suggests a background defect of unknown origin that is broader than the trace, and complicates spectral extraction at this wavelength. We therefore believe this feature is most likely spurious.

3.3.1. Supernova Emission

As a luminous long-duration GRB, we expect emission from an associated SN explosion to rise in brightness in the days following the burst. Indeed, both spectroscopic (de Ugarte Postigo et al. 2022a) and photometric (Belkin et al. 2022; Fulton et al. 2023) observations have claimed the detection of the associated SN, named SN 2022ixw. However, in contrast to these works, we do not see significant evidence for SN emission in our observations. While we lack the temporal resolution of other observations, we do have better spectral

coverage, and our SED shows little change from 0.5–55 days (Figures 2 and 6).

At later times, there also appears to be minimal spectral change in our HST observations (see Figure 6). Although our results between different methods (e.g., GALFIT versus curve of growth) are consistent, there are minor differences in the resulting photometry. It does appear that the F160W points lie slightly below the pure afterglow extrapolation in all cases, while the F098M points lie slightly above it. This would be consistent with the presence of some SN light, which should peak around the Y-band with the heavy extinction. However, there is little ability to add an optical-peaking SN component without violating the observed r-band observations.

To check this, we initially fit a simple scaling of the best-fit absorbed power law (from the JWST data) to the HST photometry obtained via 1D decomposition or GALFIT. These give χ^2/dof for each epoch of 1.1 and 0.7 for the 1D decomposition and 2.2 and 1.1 for the GALFIT models. In three out of four cases, there is little justification for the addition of a further component, although the early (30 day) HST epoch is a relatively poor fit for the GALFIT values. To quantify the possible contribution of an SN similar to SN 1998bw, we then fit a linear combination of an SN 1998bw template (via the light curves of Clocchiatti et al. 2011, supplemented with the IR observations of Patat et al. 2001). These suggest that an SN between 10%–40% of the brightness of SN 1998bw would improve the fit. However, the presence and properties of the SN remain subject to significant systematic uncertainty due to the contribution of the underlying host galaxy, which complicates precision photometry.

The light curve in the HST observations is consistent with a single power law of slope $\alpha \approx -1.5$ (although with limited coverage to distinguish any variation from a power law). Notably, this slope is consistent with optical/IR measurements made earlier in the afterglow phase. Ultimately, HST observations should provide extremely high-S/N measurements of the afterglow/SN brightness. Indeed, given some evidence for late-time energy injection in the X-ray (Williams et al. 2023), measuring changes in the spectral shape and not just the temporal decay is particularly important. For this, the host galaxy must be accurately removed, requiring late-time observations. However, for a $t^{-1.4}$ decay for the afterglow, and on the assumption that the IR was dominated by afterglow emission at 55 days post-burst, it will take a decade for the afterglow to reach F160W > 28, where we can be confident of little contribution from the SN/afterglow. It may be possible to use the differing decays of afterglow and SN (e.g., a power law versus an exponential decay from ^{56}Ni) to decompose light-curve contributions at earlier epochs, but doing so will require multiple further epochs of HST observations.

The JWST spectrum should also provide strong constraints on the presence of any SN. In particular, it is reasonably described by a single power law without requiring additional broad features from the associated SNe. SNe peak at around the rest-frame V-band, but the combination of redshift and, in particular, the heavy extinction pushes this peak into the near-IR for GRB 221009A (see, e.g., Fulton et al. 2023). In Figure 2, we plot the best-fit power law to the data after correction for the extinction. The JWST spectrum is in excess of the model at $\sim 1 \mu$m and appears to rise at the blue end. However, we caution that this region is where the afterglow is faintest and where the extinction correction is largest. However, the simultaneous GTC spectrum also shows rising flux blueward of the JWST. This may suggest that the blue upturn in JWST is accurate and has a blue SN contribution. This SN would be substantially bluer than SN 1998bw at the same epoch. Still, there is some variation in the apparent colors of SNe associated with GRBs. For example, SN 2013cq/GRB 130427A is apparently bluer (Levan et al. 2014; Melandri et al. 2014) than SN 1998bw in the optical (e.g., 4000–8000 Å) regime. This possibility will be investigated further by A. de Ugarte Postigo et al. (2023, in preparation).

Possible explanations for the differing interpretations of the SN in GRB 221009A may arise from assumptions in the afterglow model. For example, Fulton et al. (2023) assumed that the X-ray and optical lie on the same branch of the power-law spectrum (and hence decay at the same rate). The different spectral slope inferred from the JWST observations suggests this is not the case, and so the assumption of similar decay rates may not be correct. Indeed, fitted separately, the X-ray and optical regimes give different decays (see Section 5.1). Indeed, Williams et al. (2023) also found a break necessary, although they placed this break within the X-ray band. It is also possible that a rising SN component compensates for a spectral change in the afterglow. However, such an explanation would suffer from a fine-tuning problem.

4. Host Galaxy

The host galaxy of GRB 221009A is visible in our late-time HST observations. It appears to be an edge-on system with the burst close to the nuclear regions, but with a notable offset (0."25 ≈ 0.65 kpc) from the nucleus of the host. At the time of our latest

observations, there remains a substantial afterglow contribution. However, our fits with GALFITM allow us to extract reasonably robust host galaxy photometry in the case that a smooth distribution represents the entire galaxy. It is also possible (and perhaps even likely) that the distribution is not smooth due to a bright star-forming region under the GRB position. However, we report here the results based on a single Sérsic component. Our model magnitudes are F625W = 24.88 ± 0.08, F775W = 23.80 ± 0.14, F098M = 22.00 ± 0.06, F125W = 21.37 ± 0.07, and F160W = 20.92 ± 0.10.

Correction for the tabulated foreground extinction provides F625W = 21.4 or $M_{F625W} \sim -18.0$. This absolute magnitude is rather typical for a long-GRB host galaxy. In principle, the colors of the host galaxy can provide details of the stellar population within the host. However, in this case, it is complicated by the large and uncertain foreground extinction. We note that the observed colors of the source for this foreground are reasonable, with F625W−F160W(AB) ≈ 1.2 after extinction correction for the tabulated Milky Way extinction, consistent with typical colors for GRB host galaxies as a whole (Hjorth et al. 2012; Lyman et al. 2017).

Our GALFITM model also provides us with an estimate of the galaxy size. We determine an effective radius of $R_e = 2.45 \pm 0.20$ kpc for the F160W filter. In addition, using a mass-to-light ratio derived from the star-forming galaxies of the COSMOS2015 catalog (Laigle et al. 2016) at $z_{GRB} \pm 0.1$ and the GALFITM F160W magnitude corrected for extinction, we estimate a stellar mass of $\log(M_*/M_\odot) = 9.00^{-0.47}_{+0.23}$. The comparison with a star-forming population of the 3D-HST survey (Skelton et al. 2014; van der Wel et al. 2014; Momcheva et al. 2016) at a similar redshift suggests that the host size is typical for this epoch (left and right panels of Figure 8). Although, we note that this host galaxy seems to populate the lower part of the star formation rate (SFR)-weighted median of field galaxies, as previously observed for long-GRB host galaxies up to $z \sim 2$ (Kelly et al. 2014; Schneider et al. 2022). Compared to the populations of short and long-GRB hosts (right panel of Figure 8), the size of the GRB221009A host appears to be more similar to long-GRB hosts than to short GRB hosts that populate larger and more massive galaxies. For F160W, our model returned a Sérsic index of $n = 1.71 \pm 0.18$ and an axis ratio of $b/a = 0.22 \pm 0.01$, in agreement with the apparent edge-on, disk-like morphology observed in the WFC3/IR images. This morphology seems slightly more unusual among GRB hosts (Lyman et al. 2017), although some local events do appear in such galaxies. These diagnostics suggest that the host of GRB 221009A is not especially unusual among the hosts of either long- or short-duration GRBs.

The location within the host galaxy and the host galaxy characteristics appear to be very typical of long GRBs. This argues that the Galactic environment of GRB 221009A is not the cause of its extreme properties, and, in particular, there is no evidence that it was spawned in a very low-metallicity system.

5. Discussion

5.1. Implications for Afterglow Models

GRB afterglows are well described by the dynamics of a relativistic shell colliding with an external medium and synchrotron emission from the associated shocks (e.g., Sari
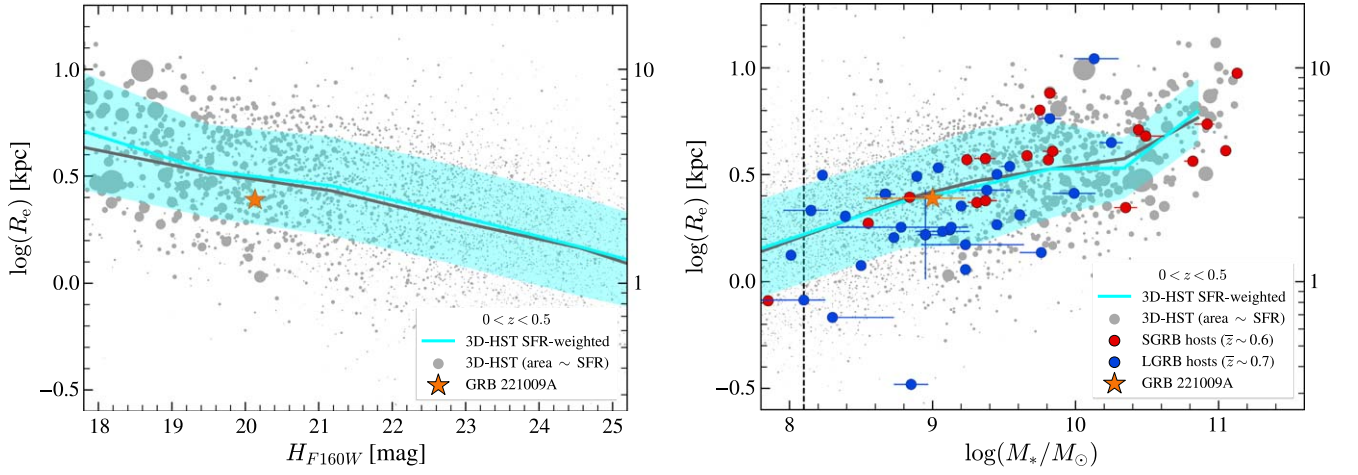
Figure 8. Effective radius as a function of F160W magnitude (left) and against stellar mass (right) for GRB hosts and 3D-HST star-forming galaxies at $0 < z < 0.5$. The red circles are a population of short GRB hosts at $z < 1$ from Fong et al. (2022) and Nugent et al. (2022), and blue circles a population of long-GRB hosts at $z < 1$ from Kelly et al. (2014) and Blanchard et al. (2016). The GRB 221009A host galaxy is visible as an orange star marker. The SFR-weighted median of the 3D-HST population and its 1σ uncertainty are shown as a cyan line and a surrounding cyan region.

et al. 1998). The physics of the broadband spectral and temporal behavior of the afterglow are linked through the various closure relations that depend on the spectral regime, observed time, and density of the external medium (Granot & Sari 2002). Changes in the observed spectral and temporal power-law indices are useful diagnostic tools; when compared with the expectation from GRB afterglow relations, they can be used to identify the spectral regime of the observed afterglow components and determine the external medium density profile —typically a uniform interstellar medium (ISM), or stellar wind.

For GRB 221009A, the spectral index changes from $\beta \sim 0.8 \pm 0.1$ at X-ray frequencies to $\beta \sim 0.3 \pm 0.1$ at NIR. This change is consistent with that expected from the cooling break (ν_c), $\beta_{\nu > \nu_c} - \beta_{\nu < \nu_c} = \Delta\beta = 0.5$, where above the cooling break frequency, synchrotron electrons will lose energy significantly. For $\nu > \nu_c$, then $\beta = p/2$, where p is the power-law index of the Lorentz factor distribution for the shock-accelerated electrons that produce the synchrotron emission. Given a spectral index of $\beta = 0.8$, we find $p = 1.6$ for $\nu > \nu_c$; where for GRB afterglows, the value of p typically lies in the range $2 \leqslant p \leqslant 3$, a value of $p < 2$ is, however, not unusual (e.g., Higgins et al. 2019). Similarly, for $\nu < \nu_c$, then $\beta = (p-1)/2$, and for $\beta = 0.3$ we find a consistent $p = 1.6$. However, the steep temporal decline of the afterglow (where $F_\nu(t) \propto \nu^{-\beta} t^{-\alpha}$), with $\alpha \sim 1.67$ at X-ray frequencies (Williams et al. 2023), and $\alpha \sim 1.44$ at optical/NIR (Shrestha et al. 2023) is not consistent with the expected decline rate, given these spectral regimes and $p < 2$ using standard closure relations. To resolve this, we invoke a very early jet break without significant lateral spreading, that steepens the temporal index by three-fourths, and the temporal index for an ISM medium with $p < 2$ is then (Gao et al. 2013)

$$\alpha_1 = \frac{3(p+6)}{16}, \quad (\nu < \nu_c) \tag{1}$$

$$\alpha_2 = \frac{3p+22}{16}, \quad (\nu > \nu_c). \tag{2}$$

These relations provide decline indices of $\alpha_2 \sim 1.675$ and $\alpha_1 \sim 1.425$ and are similar to the observed afterglow decline rates at both X-ray and optical/NIR frequencies. This result is

consistent with the "no observed SN" scenario described in Shrestha et al. (2023), where the light curve is dominated by emission from the GRB afterglow only with no significant SN contribution, and consistent with the lack of any SN features in the spectra at >10 days.

For the cooling break to be found between optical and X-ray frequencies for the duration of the observed afterglow, we require an energy on the order of 10^{54} erg, in a uniform ISM with $n \sim 1$ cm^{-3} (see, e.g., Kann et al. 2023), and fixing microphysical parameters (that describe the fraction of the shock energy that goes into the magnetic field, ε_B, and the accelerated electrons, ε_e) to $\varepsilon_B = 0.01$ and $\varepsilon_e = 0.1$ gives $\nu_c \sim 6 \times 10^{15}$ Hz, $\nu_a \sim 40$ GHz, and $\nu_m \sim 3$ GHz at ~ 0.5 days and $\nu_c \sim 10^{15}$ Hz, $\nu_a \sim 4$ GHz, and $\nu_m \sim 2$ MHz at 13 days, where ν_m is the characteristic synchrotron frequency, and ν_a is the self-absorption frequency. The spectral and temporal peak emission for the synchrotron process is at the characteristic synchrotron frequency unless $\nu_a > \nu_m$, then the spectra will peak at the self-absorption frequency. In the $p < 2$ regime, where $\nu_m < \nu_a < \nu_c$ ($\nu_a < \nu_m < \nu_c$), then $\nu_a \propto t^{-(3p+26)/[8(p+4)]}$ ($t^{-[9(p-2)]/[16(p-1)]}$), and for $p = 1.6$ we have $\nu_a \propto t^{-11/16}$ ($t^{3/8}$), and decreasing(increasing) with time. Emission below the synchrotron self-absorption frequency will be suppressed and, post-jet-break, will evolve as $t^{1/2}$ where $\nu_m < \nu < \nu_a$ (and $t^{-(14-5p)/[16(p-1)]}$ or $t^{-5/8}$ with $p = 1.6$, where $\nu < \nu_a < \nu_m$; see, e.g., Gao et al. 2013).

These spectral break frequencies are approximately consistent with the extrapolated join in the optical to X-ray spectrum (see Figure 7), and, although the self-absorption frequency is a factor of a few above that seen in early radio observations (Laskar et al. 2023), the radio peak frequency and spectral behavior is $\sim$consistent if we assume that our ν_a is under-estimated. An estimate of the maximum flux for this model ($F_{max} \sim 10$ Jy at 0.5 day, and noting that as $\nu_m < \nu_a$ the spectral peak at $\nu_a \sim 40$ GHz results in a suppressed peak flux, $F \sim 400$ mJy) and, following the closure relations in Gao et al. (2013), the flux density from a post-jet-break and $p < 2$ model evolves with time as $t^{-1.425}$ for $p = 1.6$ and $\nu_m < \nu_a < \nu$. The predicted light curve has a slightly more rapid decline than that seen in radio observations (Laskar et al. 2023); however, the reverse shock can peak at radio frequencies and may contribute to this

low-frequency emission. Alternatively, post-jet-break, the emission from higher latitudes that is given a so-called "structured jet," where significant energy extends beyond the highly collimated jet core region, can contribute to the light curve (Lamb et al. 2021); e.g., see Sato et al. (2022) and O'Connor et al. (2023), who use structured jet models to explain the irregular temporal behavior of the afterglow for this GRB. However, it is beyond the scope of this work to precisely model and fit the full afterglow light curve.

Using the estimate above for the energy and ambient density, and requiring a jet-break at <0.03 day, the time at which the light curve temporal index will steepen by three-fourths, we find a very narrow jet with a half-opening angle, $\theta_j < 0.02$ rad or $\sim 1.15°$, and a Lorentz factor, $\Gamma \sim 50$, at the jet-break time. The transition to the Newtonian regime for a decelerating blast wave occurs when $\Gamma(t) \sim \sqrt{2}$. Where $\Gamma \sim 50$ at 0.03 day, then as $\Gamma(t) \propto t^{-3/8}$, the transition to the Newtonian regime will occur on the order of ~ 1 yr.

Without the NIR spectral index of $\beta \sim 0.3 \pm 0.1$, it is tempting to assume a wind-like medium for the afterglow model (e.g., Ren et al. 2022; Laskar et al. 2023). As noted above, the change in the spectral index from higher energies to the NIR, $\Delta\beta \sim 0.5$, indicates the cooling break, ν_c, between X-ray and optical frequencies. For a wind-like medium, the temporal decline at $\nu > \nu_c$ is shallower than the decline at $\nu < \nu_c$. However, the observed light curve has a shallower decline at optical/NIR than at X-ray frequencies, which rules out the cooling break as the origin of the observed change in the spectral index if we invoke a wind-like medium (however, see the discussion in Laskar et al. 2023, for arguments in favor of a wind-like environment). Therefore, such a model requires that X-ray to NIR occupy the same spectral regime, $\nu_m < \nu < \nu_c$, giving $p \sim 2.6$ and a common temporal index at X-ray energies through optical to NIR, and contrary to the observed light-curve evolution, which differs between the optical and X-ray regimes. The spectral index at $\nu < \nu_m$ is $\beta = -1/3$, with a spectral peak that evolves with time as $\nu_m \propto t^{-3/2}$. If the recent passage of this spectral break was the cause of the $\beta \sim 0.2$ spectral index in the X-SHOOTER spectrum at ~ 0.5 days, then a chromatic break in the optical to NIR light curve, from t^0 to $t^{-1.7}$ for $p = 2.6$, would need to be present before this time—and such a change is not seen. Additionally, the ν_m spectral break is expected to be relatively sharp, unlike the cooling break (see Uhm & Zhang 2014), and should be well below the wavelength range of the JWST spectra at ~ 13 days, making the observed $\beta \sim 0.4$ at NIR difficult to explain via a wind-medium model. We, therefore, favor an early jet break, $p < 2$, uniform ISM environment, and $\nu_m < \nu_a < \nu_c$ spectral order to explain the afterglow.

5.2. Implications for the Progenitor of GRB 221009A

A striking result is an apparent absence of any SN emission in GRB 221009A. We note that this result conflicts with claims on SNe to date (Fulton et al. 2023), which are based on substantially more complete photometric coverage but lack the high-S/N spectral information presented here. In particular, in the analysis of Fulton et al. (2023), the SN should contribute essentially no light to the afterglow+SN combination at ~ 0.5 day, but $\sim 20\%$–30% at the time of the JWST observations, and $>50\%$ at the time of the HST observations. Such an SN should be visible as a marked change in the F625W-F098M color (or as an excess visible in the NIRSPEC spectrum). This is not the

case. In part, this may reflect assumptions about the afterglow's underlying spectral and temporal behavior. Isolating any SN component within this burst is not straightforward, given the issues associated with high foreground extinction and crowding.

The lack of any associated SN would be surprising within this GRB. Although there have been several long GRBs seen without apparently associated SNe (Della Valle et al. 2006; Fynbo et al. 2006; Gal-Yam et al. 2006), in most cases, these have now been suggested to arise from compact object mergers (Gehrels et al. 2006; Rastinejad et al. 2022), with evidence for kilonovae in several cases (Jin et al. 2015; Yang et al. 2015; Rastinejad et al. 2022; Troja et al. 2022; Yang et al. 2022). GRB 221009A may belong to this class. However, the energetics of GRB 221009A lie substantially beyond any seen in other merger-origin GRBs. For example, the recent GRB 211211A has $E_{\rm iso} = 7 \times 10^{51}$ erg (Mei et al. 2022; Gompertz et al. 2023), almost 3 orders of magnitude less energetic than that of GRB 221009A. The most energetic short GRBs at higher redshift also have $E_{\rm iso} \sim 5 \times 10^{52}$ erg (Fong et al. 2015).

An alternative explanation for SN-less long GRBs is that they arise from direct collapse to black holes in which insufficient material is launched into an associated shock to power a successful SN (Fynbo et al. 2006). Such events may arise in GRBs from very massive stars. If such stars have a substantial energy reservoir for the GRB, one may get a very luminous GRB without an associated SN. Very massive stars may be more common at lower metallicity. At least, stars that retain sufficient mass at later times are expected to occur more frequently at metallicities where wind-driven mass loss becomes less important (Heger et al. 2003; Fryer et al. 2019).

Finally, and perhaps most likely, GRB SNe have a modest range of luminosities, as well as evolution timescales and colors (Cano et al. 2017). Given the difficulties in isolating the GRB afterglow, host galaxy and SN light, it is plausible that an event somewhat less luminous than SN 1998bw (and perhaps somewhat faster evolving or bluer) could have evaded detection in our observations. Ultimately, once deep images are available for image subtraction, the HST photometry should allow S/N > 100 measurements of the spectral shape. We may then expect to uncover the associated SN light.

6. Conclusions

We have presented a series of high-S/N measurements of the spectral shape of the optical to mid-IR afterglow of GRB 221009A. These data, at high confidence, demonstrate that the optical/IR shape is not the same as that seen in the X-ray or as the X-ray to optical index. This suggests that the two regimes lie on different branches of the synchrotron spectrum. The separation in the spectral slopes of $\Delta\beta \sim 0.5$ makes the difference most likely due to the cooling break. However, tensions with other multiwavelength data remain, and these do not have straightforward solutions (e.g., Laskar et al. 2023; Williams et al. 2023).

The optical to mid-IR (0.6–12 μm) SED shows little evidence for variability from early to late times (0.5–55 days). The lack of variability implies, at most, modest contributions from SN emission at these epochs or that the SN emission peaks outside of the wavelength range covered (e.g., to the blue). The challenges of high foreground extinction and a bright afterglow will continue to make studying the SN associated with GRB 221009A challenging. Still, accurate host

subtraction, combined with the collation of the extensive, coherent data obtained for GRB 221009A, should enable much better constraints. It is unlikely (although possible in the absence of clear-cut evidence for an SN) that GRB 221009A is created through a compact object merger.

The burst's environment (i.e., its host galaxy) appears very broadly typical of the long-GRB population. There is no evidence of an unusual galaxy or location within the host. This, in turn, implies that the environment in which GRB 221009A formed is comparable to those of other long GRBs at low redshift. For example, it does not match where we may expect to locate very low-metallicity gas, or especially massive stars. Hence, the extreme properties of the burst are likely not linked to an extreme and unusual environment.

We dedicate this work to the memory of David Alexander Kann, whose contributions both to GRB 221009A, and to the field have been so important for the past 20 years.

Facilities: JWST(NIRSPEC/MIRI), HST (WFC3), VLT, GTC, TNG, NOEMA.

Software: astropy (Astropy Collaboration et al. 2013, 2018), emcee (Foreman-Mackey et al. 2013), GALFIT (Peng et al. 2010).

ORCID iDs

A. J. Levan ⓘ https://orcid.org/0000-0001-7821-9369
G. P. Lamb ⓘ https://orcid.org/0000-0001-5169-4143
B. Schneider ⓘ https://orcid.org/0000-0003-4876-7756
J. Hjorth ⓘ https://orcid.org/0000-0002-4571-2306
T. Zafar ⓘ https://orcid.org/0000-0003-3935-7018
A. de Ugarte Postigo ⓘ https://orcid.org/0000-0001-7717-5085
B. Sargent ⓘ https://orcid.org/0000-0001-9855-8261
S. E. Mullally ⓘ https://orcid.org/0000-0001-7106-4683
L. Izzo ⓘ https://orcid.org/0000-0001-9695-8472
P. D'Avanzo ⓘ https://orcid.org/0000-0001-7164-1508
E. Burns ⓘ https://orcid.org/0000-0002-2942-3379
J. F. Agüí Fernández ⓘ https://orcid.org/0000-0001-6991-7616
T. Barclay ⓘ https://orcid.org/0000-0001-7139-2724
M. G. Bernardini ⓘ https://orcid.org/0000-0001-6106-3046
K. Bhirombhakdi ⓘ https://orcid.org/0000-0003-0136-1281
M. Bremer ⓘ https://orcid.org/0000-0001-7511-3745
S. Campana ⓘ https://orcid.org/0000-0001-6278-1576
A. A. Chrimes ⓘ https://orcid.org/0000-0001-9842-6808
V. D'Elia ⓘ https://orcid.org/0000-0002-7320-5862
M. Della Valle ⓘ https://orcid.org/0000-0003-3142-5020
M. De Pasquale ⓘ https://orcid.org/0000-0002-4036-7419
W. Fong ⓘ https://orcid.org/0000-0002-7374-935X
A. S. Fruchter ⓘ https://orcid.org/0000-0002-6652-9279
J. P. U. Fynbo ⓘ https://orcid.org/0000-0002-8149-8298
N. Gaspari ⓘ https://orcid.org/0000-0002-3855-707X
B. P. Gompertz ⓘ https://orcid.org/0000-0002-5826-0548
D. H. Hartmann ⓘ https://orcid.org/0000-0002-8028-0991
C. L. Hedges ⓘ https://orcid.org/0000-0002-3385-8391
K. E. Heintz ⓘ https://orcid.org/0000-0002-9389-7413
K. Hotokezaka ⓘ https://orcid.org/0000-0002-2502-3730
P. Jakobsson ⓘ https://orcid.org/0000-0002-9404-5650
D. A. Kann ⓘ https://orcid.org/0000-0003-2902-3583
J. A. Kennea ⓘ https://orcid.org/0000-0002-6745-4790
T. Laskar ⓘ https://orcid.org/0000-0003-1792-2338
E. Le Floc'h ⓘ https://orcid.org/0000-0001-7421-4413
D. B. Malesani ⓘ https://orcid.org/0000-0002-7517-326X
A. Melandri ⓘ https://orcid.org/0000-0002-2810-2143
B. D. Metzger ⓘ https://orcid.org/0000-0002-4670-7509

S. R. Oates ⓘ https://orcid.org/0000-0001-9309-7873
E. Pian ⓘ https://orcid.org/0000-0001-8646-4858
S. Piranomonte ⓘ https://orcid.org/0000-0002-8875-5453
G. Pugliese ⓘ https://orcid.org/0000-0003-3457-9375
J. L. Racusin ⓘ https://orcid.org/0000-0002-4744-9898
J. C. Rastinejad ⓘ https://orcid.org/0000-0002-9267-6213
M. E. Ravasio ⓘ https://orcid.org/0000-0003-3193-4714
A. Rossi ⓘ https://orcid.org/0000-0002-8860-6538
A. Saccardi ⓘ https://orcid.org/0000-0002-6950-4587
R. Salvaterra ⓘ https://orcid.org/0000-0002-9393-8078
B. Sbarufatti ⓘ https://orcid.org/0000-0001-6620-8347
R. L. C. Starling ⓘ https://orcid.org/0000-0001-5803-2038
N. R. Tanvir ⓘ https://orcid.org/0000-0003-3274-6336
C. C. Thöne ⓘ https://orcid.org/0000-0002-7978-7648
A. J. van der Horst ⓘ https://orcid.org/0000-0001-9149-6707
S. D. Vergani ⓘ https://orcid.org/0000-0001-9398-4907
D. Watson ⓘ https://orcid.org/0000-0002-4465-8264
K. Wiersema ⓘ https://orcid.org/0000-0002-9133-7957
R. A. M. J. Wijers ⓘ https://orcid.org/0000-0002-3101-1808
Dong Xu ⓘ https://orcid.org/0000-0003-3257-9435

References

Abbott, B. P., Abbott, R., Abbott, T. D., et al. 2017, ApJL, 848, L12
Ahumada, T., Singer, L. P., Anand, S., et al. 2021, NatAs, 5, 917
Aitken, D. K. 1988, PASA, 7, 462
Astropy Collaboration, Price-Whelan, A. M., Sipőcz, B. M., et al. 2018, AJ, 156, 123
Astropy Collaboration, Robitaille, T. P., Tollerud, E. J., et al. 2013, A&A, 558, A33
Barnes, J., & Metzger, B. D. 2022, ApJL, 939, L29
Belkin, S., Moskvitin, A., Kim, V., et al. 2022, GCN, 32818, 1
Berger, E., Fong, W., & Chornock, R. 2013, ApJL, 774, L23
Bissaldi, E., Omodei, N., Kerr, M. & Fermi-LAT Team 2022, GCN, 32637, 1
Blanchard, P. K., Berger, E., & Fong, W.-f. 2016, ApJ, 817, 144
Burns, E., Svinkin, D., Fenimore, E., et al. 2023, arXiv:2302.14037
Campana, S., Mangano, V., Blustin, A. J., et al. 2006, Natur, 442, 1008
Cano, Z., Wang, S.-Q., Dai, Z.-G., & Wu, X.-F. 2017, AdAst, 2017, 8929054
Castro-Tirado, A. J., Sanchez-Ramirez, R., Hu, Y. D., et al. 2022, GCN, 32686, 1
Chapman, R., Tanvir, N. R., Priddey, R. S., & Levan, A. J. 2007, MNRAS, 382, L21
Clocchiatti, A., Suntzeff, N. B., Covarrubias, R., & Candia, P. 2011, AJ, 141, 163
de Ugarte Postigo, A., Izzo, L., Thoene, C. C., et al. 2022a, GCN, 32800, 1
de Ugarte Postigo, A., Izzo, L., Pugliese, G., et al. 2022b, GCN, 32648, 1
Della Valle, M., Chincarini, G., Panagia, N., et al. 2006, Natur, 444, 1050
Dichiara, S., Gropp, J. D., Kennea, J. A., et al. 2022, GCN, 32632, 1
Dzhappuev, D. D., Afashokov, Y. Z., Dzaparova, I. M., et al. 2022, ATel, 15669, 1
Fitzpatrick, E. L. 1999, PASP, 111, 63
Fong, W., Berger, E., Margutti, R., & Zauderer, B. A. 2015, ApJ, 815, 102
Fong, W.-f., Nugent, A. E., Dong, Y., et al. 2022, ApJ, 940, 56
Foreman-Mackey, D., Hogg, D. W., Lang, D., & Goodman, J. 2013, PASP, 125, 306
Frederiks, D., Lysenko, A., Ridnaia, A., et al. 2022, GCN, 32668, 1
Fruchter, A. S., Levan, A. J., Strolger, L., et al. 2006, Natur, 441, 463
Fryer, C. L., Lloyd-Ronning, N., Wollaeger, R., et al. 2019, EPJA, 55, 132
Fulton, M. D., Smartt, S. J., Rhodes, L., et al. 2023, arXiv:2301.11170
Fynbo, J. P. U., Watson, D., Thöne, C. C., et al. 2006, Natur, 444, 1047
Gal-Yam, A., Fox, D. B., Price, P. A., et al. 2006, Natur, 444, 1053
Gao, H., Lei, W.-H., Zou, Y.-C., Wu, X.-F., & Zhang, B. 2013, NewAR, 57, 141
Gehrels, N., Norris, J. P., Barthelmy, S. D., et al. 2006, Natur, 444, 1044
Gompertz, B. P., Levan, A. J., Tanvir, N. R., et al. 2018, ApJ, 860, 62
Gompertz, B. P., Ravasio, M. E., Nicholl, M., et al. 2023, NatAs, 7, 67
Gotz, D., Mereghetti, S., Savchenko, V., et al. 2022, GCN, 32660, 1

Granot, J., & Sari, R. 2002, ApJ, 568, 820
Häußler, B., Bamford, S. P., Vika, M., et al. 2013, MNRAS, 430, 330
Heger, A., Fryer, C. L., Woosley, S. E., Langer, N., & Hartmann, D. H. 2003, ApJ, 591, 288
Higgins, A. B., van der Horst, A. J., Starling, R. L. C., et al. 2019, MNRAS, 484, 5245
Hjorth, J., Malesani, D., Jakobsson, P., et al. 2012, ApJ, 756, 187
Hjorth, J., Sollerman, J., Møller, P., et al. 2003, Natur, 423, 847
Holwerda, B. W., Keel, W. C., Kenworthy, M. A., & Mack, K. J. 2015, MNRAS, 451, 2390
Hotokezaka, K., Tanaka, M., Kato, D., & Gaigalas, G. 2022, MNRAS, 515, L89
Huang, Y., Hu, S., Chen, S., et al. 2022, GCN, 32677, 1
Jakobsen, P., Ferruit, P., Alves de Oliveira, C., et al. 2022, A&A, 661, A80
Jin, Z.-P., Li, X., Cano, Z., et al. 2015, ApJL, 811, L22
Kann, D. A., Agayeva, S., Aivazyan, V., et al. 2023, arXiv:2302.06225
Kelly, P. L., Filippenko, A. V., Modjaz, M., & Kocevski, D. 2014, ApJ, 789, 23
Kennea, J. A., Williams, M. & Swift Team 2022, GCN, 32635, 1
Kouveliotou, C., Meegan, C. A., Fishman, G. J., et al. 1993, ApJL, 413, L101
Laigle, C., McCracken, H. J., Ilbert, O., et al. 2016, ApJS, 224, 24
Lamb, G. P., Kann, D. A., Fernández, J. J., et al. 2021, MNRAS, 506, 4163
Lamb, G. P., Tanvir, N. R., Levan, A. J., et al. 2019, ApJ, 883, 48
Lapshov, I., Molkov, S., Mereminsky, I., et al. 2022, GCN, 32663, 1
Laskar, T., Alexander, K. D., Margutti, R., et al. 2023, arXiv:2302.04388
Levan, A., Crowther, P., de Grijs, R., et al. 2016, SSRv, 202, 33
Levan, A. J., Tanvir, N. R., Fruchter, A. S., et al. 2014, ApJ, 792, 115
Liu, J. C., Zhang, Y. Q., Xiong, S. L., et al. 2022, GCN, 32751, 1
Lyman, J. D., Levan, A. J., Tanvir, N. R., et al. 2017, MNRAS, 467, 1795
Malesani, D. B., Levan, A. J., Izzo, L., et al. 2023, arXiv:2302.07891
Mei, A., Banerjee, B., Oganesyan, G., et al. 2022, Natur, 612, 236
Melandri, A., Pian, E., D'Elia, V., et al. 2014, A&A, 567, A29
Mitchell, L. J., Phlips, B. F., & Johnson, W. N. 2022, GCN, 32746, 1
Momcheva, I. G., Brammer, G. B., van Dokkum, P. G., et al. 2016, ApJS, 225, 27
Nakamura, T., Mazzali, P. A., Nomoto, K., & Iwamoto, K. 2001, ApJ, 550, 991
Nugent, A. E., Fong, W.-F., Dong, Y., et al. 2022, ApJ, 940, 57
O'Connor, B., Troja, E., Ryan, G., et al. 2023, arXiv:2302.07906
Patat, F., Cappellaro, E., Danziger, J., et al. 2001, ApJ, 555, 900
Peng, C. Y., Ho, L. C., Impey, C. D., & Rix, H.-W. 2010, AJ, 139, 2097
Piano, G., Verrecchia, F., Bulgarelli, A., et al. 2022, GCN, 32657, 1
Rastinejad, J. C., Fong, W., Kilpatrick, C. D., et al. 2021, ApJ, 916, 89
Rastinejad, J. C., Gompertz, B. P., Levan, A. J., et al. 2022, Natur, 612, 223
Ren, J., Wang, Y., & Zhang, L.-L. 2022, arXiv:2210.10673
Rieke, G. H., Wright, G. S., Böker, T., et al. 2015, PASP, 127, 584
Ripa, J., Pal, A., Werner, N., et al. 2022, GCN, 32685, 1
Rossi, A., Rothberg, B., Palazzi, E., et al. 2022, ApJ, 932, 1
Sari, R., Piran, T., & Narayan, R. 1998, ApJL, 497, L17
Sato, Y., Murase, K., Ohira, Y., & Yamazaki, R. 2022, arXiv:2212.09266
Schlafly, E. F., & Finkbeiner, D. P. 2011, ApJ, 737, 103
Schneider, B., Le Floc'h, E., Arabsalmani, M., Vergani, S. D., & Palmerio, J. T. 2022, A&A, 666, A14
Shrestha, M., Sand, D. J., Alexander, K. D., et al. 2023, arXiv:2302.03829
Siegel, D. M., Barnes, J., & Metzger, B. D. 2019, Natur, 569, 241
Skelton, R. E., Whitaker, K. E., Momcheva, I. G., et al. 2014, ApJS, 214, 24
Soderberg, A. M., Kulkarni, S. R., Nakar, E., et al. 2006, Natur, 442, 1014
Stetson, P. B. 1987, PASP, 99, 191
Tan, W. J., Li, C. K., Ge, M. Y., et al. 2022, ATel, 15660, 1
Tanvir, N. R., Levan, A. J., Fruchter, A. S., et al. 2013, Natur, 500, 547
Troja, E., Fryer, C. L., O'Connor, B., et al. 2022, Natur, 612, 228
Uhm, Z. L., & Zhang, B. 2014, ApJ, 780, 82
Ursi, A., Panebianco, G., Pittori, C., et al. 2022, GCN, 32650, 1
van der Wel, A., Franx, M., van Dokkum, P. G., et al. 2014, ApJ, 788, 28
Veres, P., Burns, E., Bissaldi, E., et al. 2022, GCN, 32636, 1
Vika, M., Bamford, S. P., Häußler, B., et al. 2013, MNRAS, 435, 623
Waxman, E., Mészáros, P., & Campana, S. 2007, ApJ, 667, 351
Williams, M. A., Kennea, J. A., Dichiara, S., et al. 2023, arXiv:2302.03642
Xiao, H., Krucker, S., & Daniel, R. 2022, GCN, 32661, 1
Yang, B., Jin, Z.-P., Li, X., et al. 2015, NatCo, 6, 7323
Yang, J., Ai, S., Zhang, B.-B., et al. 2022, Natur, 612, 232